Research Update: Distribution and stabilization of Pd catalysts in porous carbon-based supports by aggregation of pre-doped colloidal particles

Anna Beltzung,[1] Mark A. Newton,[1] Maarten Nachtegaal,[2] Hua Wu,[1] Giuseppe Storti,[1] and Massimo Morbidelli[1,a]
[1]*Department of Chemistry and Applied Biosciences, Institute for Chemical and Bioengineering, ETH Zurich, Switzerland*
[2]*Paul Scherrer Institute, 5232 Villigen, Switzerland*

(Received 29 June 2018; accepted 8 October 2018; published online 23 October 2018)

In this work, the synthesis of a stable supported Pd catalyst by aggregation of colloidal particles (CPs) of polyacrylonitrile (PAN) containing the noble metal is discussed. The metal is initially incorporated during the polymerization reaction (0.5 wt. %) and results to be well embedded inside the polymeric structure and anchored to the nitrogen atom of acrylonitrile. Moreover, aiming to provide free access towards the catalyst active sites, a KOH-activated heat treatment was performed on the PAN CP aggregates, thus creating pore sizes between 0.7 and 5 nm with surface area S_{BET} = 1150 m^2/g. After the harsh heat treatment, the amount of Pd remaining in the pyrolyzed polymer is 2.8 wt. %, as measured by Inductively Coupled Plasma-Optical Emission Spectroscopy (ICP-OES), which then corresponds to a total weight loss of 83% (assuming no loss of Pd). This result indicates a remarkable stability of Pd inside the polymer structure and that minimal Pd leaching can be expected during the catalyst use. X-ray absorption spectroscopic studies of pyrolyzed Pd-containing PAN and following extended X-ray absorption fine structure fitting showed no sign of bulk Pd(0), while a dominant proportion of Pd is present as dispersed Pd carbides. These results are consistent with the data obtained using X-ray absorption near edge structure. Finally, the catalyst was tested on a Suzuki coupling in the liquid phase and showed good activity, hence proving the accessibility of the active sites to reactants. https://doi.org/10.1063/1.5046552

I. INTRODUCTION

At the frontier between heterogeneous and homogenous catalysis, metallic nanoparticles have found a significant role.[1] Their homogeneous properties, like their availability, chemical nature, acidity, and redox properties, make them predictable and permit a "structure-activity" understanding of the catalysis.[2] Moreover, as noble metals are usually the most active in catalysis, the cost of purely metallic nanoparticles is very high and the waste of the unused metal, i.e., active species that are not on the surface of the nanoparticles, opens other doors to improvement. Alternatively, supported catalysts which are usually prepared by wet-impregnation on different oxides, charcoal, or zeolites can help "diluting" the metal homogeneously on the support while enhancing the thermal stability.[3,4] The challenge is to reduce the size and increase the monodispersity of the active sites while making them as available as possible on the surface of the support. However, metal-supported catalysts commonly suffer from sintering, which leads to deactivation, as well as selectivity issues.[5] As a consequence, many processes are still being run based

[a]Author to whom correspondence should be addressed: massimo.morbidelli@chem.ethz.ch

on homogeneous catalysis, for example, cross coupling reactions like Wacker, Cativa, or Suzuki reactions.[6]

Focusing on tailoring metal nanoparticles for supported catalysts, many studies have shown that controlling the size of the impregnated/incorporated/precipitated active sites results in different catalytic properties.[7,8] Abbot *et al.* reported the effect of the size of Pd_n clusters (n = 1–30 atoms) and found that extremely small clusters are much more effective than bigger clusters to enable the cyclotrimerization of acetylene to benzene, especially at low temperature.[9] Given the good results of metal catalysis with the active species dispersed at the atomic level, many efforts have been made to synthetize single atoms distributed on a support to achieve a high reactive efficiency per atom and similar selectivity for homogeneous catalysis, but without the drawbacks mentioned above.[10–13] However, the major drawback of such supported catalysts is that their single sites are usually not very stable.[14] In some cases, due to spatial segregation, single-site catalysis becomes ineffective when the reaction involves the anchoring of several molecules next to each other (multi-adsorption sites), as is the case in hydrogenation reactions.[15] Hence, small multi-atom clusters (2-10 atoms) also show interesting properties without the "loss" of active sites as all of their atoms are facing the surface. For example, it was reported that the number of Pt atoms (from 5 to 12) in a cluster changes the activity and selectivity of a catalyzed reaction, with the clusters of 10 atoms having the highest catalytic activity for the styrene hydrogenation reaction.[16]

The choice of a specific support is another important aspect in catalyst design as this will depend on the reaction conditions to be used and the affinity of the support material towards the active sites. In fact, the support could also play a role in the catalyst activity like in CO_2-to-methanol conversion over zirconia-supported copper nanoparticles.[17] If chemical resistance is needed, carbon-based materials are preferred, whereas metal oxides are usually very resistant towards high temperature and pressure.[18–20] For targeting a possible industrial application, the support should exhibit high loading capacity with good and preferably tailored porosity, as well as an acceptable cost of production. For this purpose, researchers have investigated the use of polymer-based materials as support for noble metal catalysis.[21,22] Their ease of production and mechanical and thermal properties, as well as the versatility in their architecture and compositions, make them candidates with good potential.[23,24] In particular, polyacrylonitrile (PAN) possesses a nitrogen heteroatom in its repeating unit, which can anchor metal compounds. Notably, after thermal treatment, PAN can form a microporous N-doped graphitic material without the need of additional nitrogen incorporation steps, as it is done with ammonia or ion implantation.[25,26] As PAN serves as a precursor for the production of very stable carbon fibers,[27] the polymeric structure, once thermally treated, provides the necessary thermal and mechanical strength to become a successful catalyst support.[28]

Herein, we described the development of a catalyst based on porous PAN colloidal particles (CPs) containing palladium prepared through the approach reported elsewhere.[29] Differing from the conventional wet-impregnation, which typically leads to the formation of metal clusters on the support, this new approach enables the *in situ* homogeneous incorporation of stable chemically bonded Pd atoms inside polymeric CPs. The scalable and reproducible dispersion of Pd-containing CPs produced by emulsion polymerization was destabilized to form a fractal-based assembly exhibiting large enough pores to minimize any diffusion limitation. Much smaller pores giving access to the palladium present inside the (originally non-porous) PAN CPs were created by a KOH-activated heat treatment, resulting in a carbon-based ladder structure. The produced catalyst shows outstanding thermal and chemical resistance, and the Pd inside the CPs is present in small aggregates (<5 nm) and probably single Pd atoms, which are still anchored to the residual nitrogen remaining in the matrix after the thermal treatment. Hence, the highly porous, graphitic-like support is helpful in stabilizing the metal. Additionally, leaching of Pd is negligible, as the amount of Pd after the harsh heat treatment involving KOH followed by acid washing is still 2.8 wt. %. Finally, its activity was tested on a Suzuki coupling in water and compared to that achieved using pure Pd nanoparticles as well as a similar catalyst synthesized by wet impregnation of the same thermally treated polymer matrix using a Pd precursor.

II. EXPERIMENTAL SECTION

A. Materials

For polymerization, the acrylonitrile (AN) monomer was purchased from Aldrich Chemicals (≥99.0%) and potassium persulfate (KPS) was employed as a water-soluble initiator and was purchased from Merck (ACS, Reag. Ph. Eur). Deionized water was used as the reaction medium for all reactions, and sodium dodecyl sulfate (SDS, Sigma Life Science, ≥99.0% purity) and potassium poly(ethylene glycol) 4-nonylphenyl 3-sulfopropylether (KPE, Sigma-Aldrich, ≥99.0% purity) were used as ionic surfactants. K_2PdCl_4, purchased from ABCR-chemicals (98% purity), was used as the palladium source. Suzuki couplings were performed using 4-bromotoluene (ABCR-chemicals, 98%), phenylboronic acid (Acros Organics, 98+ %), and *N*,*N*-Diisopropylethylamine (Fluka, ≥98%). Palladium nanoparticles (d < 25 nm) were purchased from Aldrich Chemicals with >99.5% metal basis, for direct comparison with our synthesized catalysts. All purchased raw materials were employed without further purifications. The deionized water was stripped with N_2 (bubbled through the solution) for 30 min to remove oxygen and prevent any deactivation of the initiator during the reaction.

B. Synthesis of Pd-containing PAN colloidal particles

The introduction of palladium in the colloidal particles (abbreviated as CPs) was performed during emulsion polymerization, following the recipe reported in a previous study (feeding strategy F1b).[29] In short, water, SDS, KPS, and monomers were charged to the reactor, whereas KPE and metal-precursor, both diluted in water, were fed as soon as the nucleation has started (few minutes after the initiator injection, recognizable by the appearance of a bluish color). The reaction was carried out for approximately 4 h at 60 °C with a stirring rate of 400 rpm, while reaching at least 90% conversion.

The produced latex (10% polymeric solid content) was destabilized under stagnant conditions by the addition of salt (0.1 M $CaCl_2$, until 8 wt. % dilution, 3 h in a 60 °C water bath). The resulting polymer gel was dried and sieved into clusters of size from 450 to 560 μm. The extent of the Pd-incorporation was measured quantitatively by Inductively Coupled Plasma-Optical Emission Spectroscopy (ICP-OES) and qualitatively by Scanning Transmission Electron Microscopy-Energy Dispersive X-ray Spectroscopy (STEM-EDX) mapping on the latex and reported in a previous study.[29] The obtained material was named PANPd at this stage of the synthesis.

C. Thermal treatment of PANPd

Based on previous studies on pure PAN,[28] micropores inside the CPs were created by a suitable series of thermal treatments. Such pores are expected to expose the active metal and provide access to the reactants. The first step of such a treatment was oxidation of the powder in a tubular oven (Borel, Switzerland) in air flow (100 ml/min) with the temperature ramp from room to T_O = 240 °C at a rate of 300 °C/h and a plateau at the oxidation temperature for 4 h. Directly following oxidation, the stabilization step requires 1 h of nitrogen flow (250 ml/min) at T_O to flush oxygen out of the reactor, followed by increasing the temperature to T_S = 350 °C while keeping the same nitrogen flow. After a plateau of 3 h under these conditions, the material is fully stabilized and the spherical shape of the CPs is retained. Then, the last step is applied (pyrolysis) after the addition of KOH in a 1:2 ratio (stabilized PAN:KOH). For this purpose, the weighted KOH in the form of pellets was first crushed in a mortar, then the stabilized powder was added, and both were mixed by hand for several minutes. The rather "sticky" mixture was then put on a ceramic plate, which was placed in the middle region of the tube of the oven, where the temperature is the most stable. The pyrolysis was performed increasing the temperature from room temperature to 800 °C at a rate of 400 °C/h and applying the plateau temperature for 6 h under nitrogen flow (250 ml/min). The pyrolyzed polymer was then recovered and washed with 10 ml of a 10 wt. % HCl solution for 4 h at room temperature under continuous stirring. Three additional washings with fresh HCl were also performed, and after one washing lasting 4 h, no difference in porosity was observed (for more details, see the supplementary material, Fig. 3S). Filtration was employed to recover the powder, which was washed

several times with the deionized water. Subsequently, the wet powder was placed in a vacuum oven at 50 °C for drying and then stored. The obtained material was named PANPd PYR at this stage of synthesis.

Before any reaction application, the powder was reduced using 10 mg $NaBH_4$ dissolved in 10 ml deionized water. The slurry was stirred for 4 h and filtered, and the recovered solid was washed several times with water. Subsequently, the wet powder was dried in a vacuum oven at 50 °C overnight and used on the following day for catalysis to avoid any possible oxidation of palladium prior to reaction. This catalyst was named C1 throughout this work.

D. Synthesis of the wet-impregnated catalyst

Another type of catalyst was synthesized by thermally treating PAN CPs without metal using conventional pyrolysis followed by wet impregnation with K_2PdCl_4. More details on the support synthesis, i.e., about the production of microporous pyrolyzed PAN, can be found elsewhere.[28] The impregnation was performed by adding the microporous powder to the K_2PdCl_4 aqueous solution and stirring for 2 days. Using this method, two similar catalysts were prepared with different Pd-loadings: 3.5 and 8 wt. %. Similar to C1, the Pd-containing powder was filtered, washed, and reduced. This wet-impregnated catalyst was named C2 throughout this work, with specified loading.

The synthesis path of both catalysts is depicted in Fig. 1. On the right, *in situ* incorporation of palladium inside PAN colloidal particles (catalyst C1) is represented while on the left, the wet-impregnated catalyst using pyrolyzed PAN nanoparticles (catalyst C2) is shown.

E. Characterization

Aiming to test the thermal stability of PANPd and wet-impregnated catalysts over time, approximately 10 mg of each sample were placed in two separate ceramic crucibles and put in the same tubular oven used for pyrolysis. The final temperature of 400 °C was reached in 2 h and was kept constant for 100 h under continuous N_2 flow (250 ml/min). This test was repeated twice with a cooling step to room temperature in between.

Electron microscopy measurements were performed on a FEI Talos F200X electron microscope equipped with a Super-X SDD detector at an acceleration voltage of 200 kV. EDX hypermaps were acquired in 10 min using Esprit software at the 40 keV energy range to assess the M, L, and K lines of palladium. The combination of the electron microscopy and EDX provides the distribution of the metal atom in the material. The solid powder was directly placed on a standard TEM-grid (lacey carbon film 300 mesh, Lucerna-Chem, Switzerland).

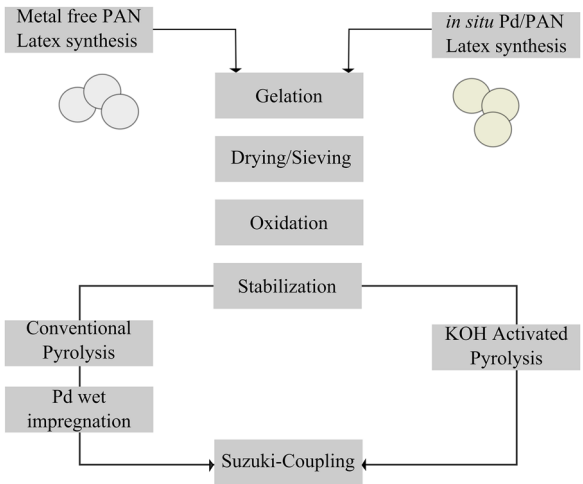

FIG. 1. Synthesis overview of the two different paths employed for the Suzuki coupling: *in situ* Pd/PAN (right) and wet impregnated (left) catalysts.

The porosity of the catalyst was also characterized by N_2-adsorption at 77 K with an ASAP 2060 (Micromeritics, USA) which results in S_{BET} and full Pore Size Distribution (PSD). A more refined size analysis of the smallest pores was carried out by CO_2-adsorption at 273 K using a Quadrasorb (Quantachrome, USA). Both PSDs were assessed assuming slit pore geometry on carbon and modelled with Density Functional Theory (DFT model, provided by the software).

Ultraviolet-Visible (UV-vis) spectra were recorded with a resolution of 1 nm in transmission mode on an Agilent Technologies, Cary Series spectrometer using dimethyl sulfoxide (DMSO) as a reference. On the same spectrometer, the diffuse reflectance Ultraviolet-Visible (UV-vis) spectra of the polymer powders with and without palladium were recorded using KBr as a reference.

X-ray absorption spectroscopy (XAS) spectra at the Pd K edge were collected at the Swiss Light Source (Paul Scherrer Institute, Switzerland). The XAS is operated at 2.4 GeV in top up mode, with a ring current of 400 mA. The polychromatic X-ray beam resulting from the 2.9 T bending magnet was collimated by a collimating mirror, monochromatized by using a Si(311) channel cut monochromator for measurements at the Pd K-edge, and subsequently focused by a toroidal mirror. The spot size on the sample measured 2×0.4 mm (H × V). On both mirrors, a Pt coating was selected for measurements at the Pd K-edge. The energy was calibrated by setting the monochromator energy to 24 350 eV at the inflection point of a Pd foil. Samples were measured in transmission mode using 20 cm long ionization chambers (filled with a mixture of Ar and N_2 for measurements at the Pd K-edge). PANPd PYR (non-reduced sample) was pressed in the form of a pellet for analysis, while the Pd foil was simultaneously measured as an absolute reference. The Pd sample was measured in fluorescence mode using a silicon drift detector with a 1 mm thick sensor. Data reduction and fitting were performed using PAXAS and EXCURV (9.3), respectively.[30,31] All spectra were background corrected and normalized. The energy units (eV) were then converted to photoelectron wave vector k units ($Å^{-1}$) by assigning the photoelectron energy origin, E_0, corresponding to $k = 0$, to the first inflection point of the absorption edge. The resulting $\chi(k)$ functions were weighted with k^3 and then Fourier-transformed to obtain pseudo radial structure functions (RSFs). The amplitude reduction factor (AFAC) was obtained from fitting the Pd-foil, i.e., 0.9. The final fit of PANPd PYR was made over the k-range 3.0–12.8 $Å^{-1}$ by adding shells stepwise, which significantly improved the fit to both k^3-weighted data and Fourier transform. The scattering paths used for the different shells were Pd–O, Pd–C, and Pd–Pd.

F. Catalytic Suzuki coupling test

Suzuki coupling was performed based on a recipe published elsewhere.[32] In a glass reactor with reflux, 1 mmol (0.326 g) of 4-bromotoluene, 1.5 mmol (0.366 g) of benzeneboronic acid, 3.0 mmol (0.776 g) of *N*,*N*-Diisopropylethylamine (Hünig Base), 9 ml deionized water, and 20 mg of the reduced catalyst were added. The reaction was performed at 90 °C and 300 rpm for 20 h, and the overall chemical reaction is represented in Fig. 2. After the completion of the reaction, 2×25 g of diethyl ether were added to the reactor and the mixture was transferred to a bottle. The 2 phase-system and the catalyst were stirred overnight to ensure full extraction of the product from the water phase and trapped inside the catalyst pores. After filtration of the catalyst, the water phase was separated using a decanter and the product was recovered after full evaporation of the solvent. The pure Suzuki product was identified after separating it from the reactants via liquid chromatography (standard percolation column) using hexane as the carrier solvent. The conversion X_p of the limiting reactant (aryl bromide) was assessed by ^{1}H NMR in $CDCl_3$. It was calculated from the area below the peaks corresponding to the methyl-group of products (A_P) and reactants (A_R). The reported

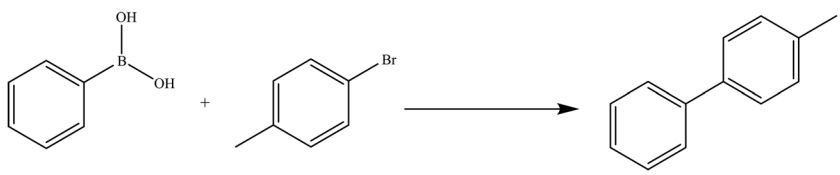

FIG. 2. Overall chemical reaction of the investigated Suzuki coupling.

ratio in Eq. (1) describes the obtained product mass (m_P) normalized with respect to the palladium mass (m_{Pd}),

$$R = \frac{\frac{A_P}{A_P+A_R} m_R}{m_{Pd}} = \frac{X_p m_R}{m_{Pd}} = \frac{m_P}{m_{Pd}}. \quad (1)$$

In addition to the comparative evaluation of these two catalysts, the same reaction was also performed using a catalyst made of pure Pd nanoparticles (diameter of nanoparticles <25 nm). The amount of nanoparticles was calculated in order to provide the quantity of metal corresponding to the C2 catalyst. These comparative results can be found in the supplementary material.

III. RESULTS

A. *In situ* Pd-incorporated PAN

Incorporation of palladium inside the PAN colloidal particles was performed during the polymerization, and hence, this permits the complete embedding of the metal-precursor in the polymer matrix. In addition, the chemical affinity between acrylonitrile and K_2PdCl_4, proved by the fast diffusion of the latter from the water phase to the micelles/polymer CPs, is beneficial for the metal stability during the following thermal treatment and, more important, in view of the catalytic applications. After the polymerization reaction, the destabilization of the Pd-containing CPs led to the formation of a macroporous gel with the pore size of 1-2 μm among the particles.[33] However, these same pores partially collapse during the next drying, thus resulting in a final material with a smaller pore size of about 100 nm.

Insights into the complex formation between Pd and AN, and the final metal coordination inside the polymer are provided by the results in Fig. 3, where the UV-vis spectra of the complex formation between the Pd-precursor and the monomer in DMSO [Fig. 3(a)] and the solid state UV-vis spectra of PAN containing palladium compared to metal-free PAN [Fig. 3(b)] are reported. The bands between 200 and 300 nm are representative of a Pd(II) d^8 complex, typically exhibiting a square-planar structure.[34–37] The spectrum of K_2PdCl_4 (black dotted line) has an absorption peak at 303 nm while acrylonitrile exhibits a peak at 255 nm (blue solid line) corresponding to the transition $\pi \rightarrow \pi^*$ of the C≡N bond.[38] After the formation of the complexes, the peak of the acrylonitrile-K_2PdCl_4 spectrum (red dotted-dashed line) shifted from 255 to 262 nm, while the Pd(II) band stays constant at 303 nm. This indicates that the oxidation state does not change during complexation and that the Pd(II) binds to the monomer. The spectra of PAN-based powders in Fig. 3(b) indicate that PAN (metal-free, black dotted line) has an absorption peak at 272 nm attributed to the C≡N π-adsorption also present in PANPd (red dotted-dashed line), which is well in line with the reported data.[39] Moreover, the PANPd spectrum reveals the presence of two characteristic maximal absorption

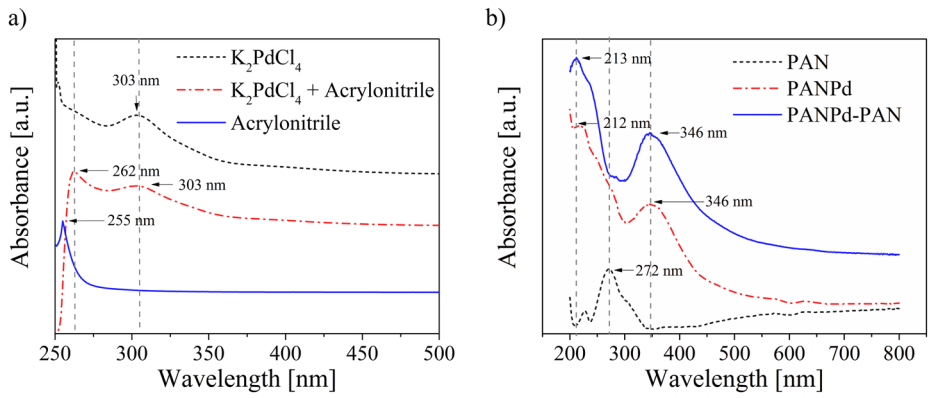

FIG. 3. (a) Liquid state UV-vis spectra of K_2PdCl_4 (black dotted line), K_2PdCl_4 and AN (red dotted-dashed line), and only AN (blue solid line) (0.1 mM in DMSO); (b) solid state UV-vis of PANPd (red dotted-dashed line) and Pd-free PAN (black dotted line) powders using KBr as the background. The PANPd-PAN spectrum (blue solid line) is the difference between PAN and PANPd spectra.

bands of Pd(II) at wavelengths λ = 212 and 346 nm, respectively. The subtraction of pure PAN from the PANPd spectra leads to the same absorbance peak, corresponding well to the Pd signal (blue solid line).

The charge transfer (CT) band at 346 nm probably corresponds to the Pd–Cl charge transfer.[40] Additionally, the absence of d-d bands is attributed to an important presence of chlorine in the coordination sphere of palladium, which is in line with the Cl-rich chemical structure of K_2PdCl_4. Finally, the CT band at 213 nm could be the result of Pd-N charge transfer, given the knowledge of the materials used in this system, e.g., acrylonitrile and K_2PdCl_4.

B. Thermal treatment

The synthesis of C1, based on *in situ* Pd latex synthesis, and C2, based on wet impregnated Pd, catalysts involves a thermal treatment in both cases. It consisted in three subsequent steps, oxidation, stabilization, and pyrolysis, where microporosity was finally introduced. However, C1 was thermally treated after the Pd incorporation while C2 was treated before the wet-impregnation. More specifically, C2 was synthesized by using the clusters of PAN CPs followed by stabilization (T_O = 240 °C, T_S = 350 °C) and conventional pyrolysis (900 °C). This type of pyrolysis results in the formation of narrow micropores (0.35–0.7 nm) inside each individual nanoparticle, which are large enough for the fast diffusion of gaseous species but too small for liquid species.

The STEM-EDX map of the targeted 3.5 wt. % Pd loading C2 catalyst is shown in Fig. 4(a). The wet-impregnation of Pd on pyrolyzed PAN clusters of nanoparticles followed by reduction resulted in a distribution of Pd nanoparticles on the surface. The difference in densities between the pyrolyzed polymer and the palladium is responsible for the brighter spots, corresponding to Pd(0) nanoparticles. Such metal nanoparticles seem predominantly small (5-10 nm) even though a few, bigger particles can also be observed (20-30 nm). Higher metal loading of the C2-type material (8 wt. %) leads to the dominant presence of bigger nanoparticles, as can be seen in the palladium STEM-EDX in Fig. 5. As the support is the same for both loadings, hence also the porosity, only the distribution of Pd at the surface is affected by the different loading.

The Pd nanoparticles on the surface of C2 are fully accessible, even though the Pd atoms buried inside the nanoparticles themselves cannot be reached by the reactants and, therefore, will never be effective to catalyze reactions. The pore size distributions based on CO_2-adsorption at 273 K and high vacuum ($p/p_0 < 0.01$, microporous monolayer) and N_2-adsorption at 77 K are depicted in Fig. 4(b). Thanks to the hydrodynamic radius of the CO_2 molecule (0.33 nm) and the higher

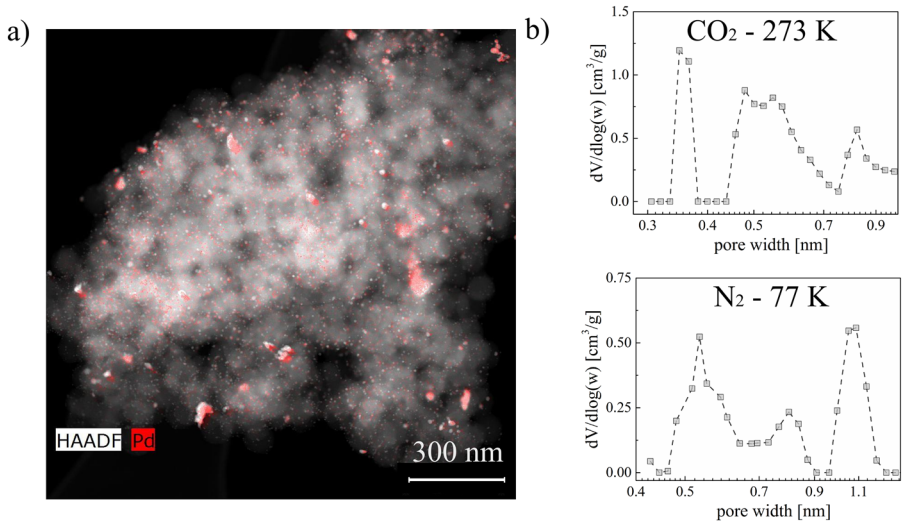

FIG. 4. C2 wet-impregnated PAN-Pd catalyst with a target loading of 3.5 wt. % Pd. (a) STEM-EDX of Pd Lα lines after wet-impregnation and reduction; (b) pore size distribution using DFT model based on CO_2-adsorption (top) and N_2-adsorption (bottom).

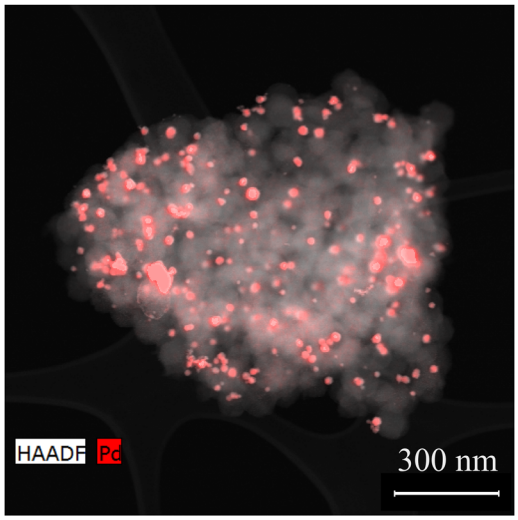

FIG. 5. STEM-EDX (Pd Lα lines) of the C2 catalyst after wet-impregnation and reduction with a target loading of 8 wt. % Pd.

operating temperature—pores up to 0.35 nm can be assessed in the first case. The PSD based on CO_2 and N_2 showed another set of pores, whose size is ranging between 0.5 and 0.9 nm. As previously mentioned, these pores are useful for gaseous applications, like CO_2 capture, but do not permit fast enough diffusion of reactants and products in the liquid phase. Moreover, in terms of overall porosity, the BET surface area (S_{BET}) measured by N_2-adsorption at 77 K for Pd-free PAN CPs assemblies after conventional pyrolysis was 358 m^2/g, while the same material exhibited a S_{BET} of 40 m^2/g after wet-impregnation and drying. Even though the BET equation is not the most reliable tool for assessing microporous materials, it is still useful for material comparison. The decrease in surface area is probably due to the filling of middle-size pores by $[PdCl_4]^{2-}$ aggregates, thus blocking the entries of smaller pores to N_2 molecules.

In the case of the C1 catalyst, conventional pyrolysis is not sufficient in providing the necessary pore size for high catalytic activity, and thus, KOH activated pyrolysis (KAP) was performed. As already reported, KOH is employed to enhance the formation of large pores, thus increasing the surface area and, in our case, the accessibility to the metal.[41–44] Moreover, weight loss resulting from KAP is not negligible (83%) and thus the pyrolysis temperature should be carefully assessed. For this last step of the heat treatment, a temperature of 800 °C was found ideal to avoid too much weight loss while achieving high surface areas.

The STEM-EDX mapping of the Pd-incorporated catalyst C1 is shown in Fig. 6(a). The palladium seems homogeneously distributed in the pyrolyzed polymer, and no major aggregation, i.e., no brighter spots, seems to have taken place. From the PSD in Fig. 6(b), it is clear that the goal of creating larger pore sizes was achieved as more micropore volume based on the CO_2-adsorption [Fig. 6(b) top] was created between 0.5 and 0.9 nm. In the case of the PSD based on N_2-adsorption [Fig. 6(b) bottom], the distribution has also shifted towards bigger pores and a differential volume of almost 3 cm^3/g was achieved for pore sizes between 0.9 and 1.2 nm, in comparison with 0.5 cm^3/g for the C2 catalyst [Fig. 4(b), bottom]. A recapitulation of the applied thermal treatments and the corresponding metal loading and surface area is provided in Table I. Catalyst C1 was synthetized following the KAP treatment while the preparation of C2 involved the wet-impregnation treatment comprising a conventional pyrolysis step. For clarity, the conventional pyrolysis (Conv. Pyrolysis) treatment alone is depicted in Table I for the sake of S_{BET} comparison.

The S_{BET} values of the different samples could be assessed by measuring the full N_2-adsorption isotherm (see Fig. 2S of the supplementary material). As we can see from Table I, the main difference between KAP and treatments involving conventional pyrolysis is the use of KOH, whose presence leads to higher weight loss and requires suitable post-treatments (repeated HCl-washing, filtration, etc.) which could remove the metal or induce its aggregation.

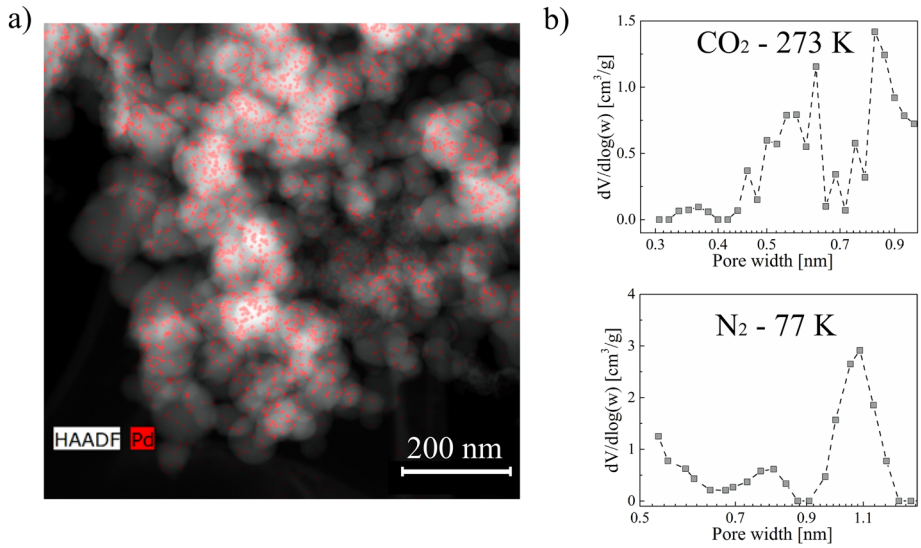

FIG. 6. C1 catalyst: (a) STEM-EDX (Pd Lα lines) after KAP, Pd Lα, enhanced signals and (b) pore size distribution after KAP using DFT model based on CO_2-adsorption at 273 K (top) and N_2-adsorption at 77 K (bottom).

TABLE I. Different thermal treatments and their conditions (KOH amount, temperature of pyrolysis, T_P) and resulting Pd loading and surface area (S_{BET}).

Type of treatment	KOH/stabilized PAN ratio (–)	T_P (°C)	Pd (wt. %)	S_{BET} (m^2/g)
Conv. Pyrolysis[a]	0	900	0	358
Wet-impregnation (C2)	0	900	3.5	40
KAP (C1)[b]	2	800	2.8	1150

[a]Conv. = conventional.
[b]KAP = KOH activated pyrolysis.

Besides the surface area, the main difference between reduced PANPd PYR (C1) and the wet-impregnated (3.5 Pd wt. %) (C2) catalysts is the spatial distribution of the metal, as shown in Figs. 4(a) and 6(a). In C1, the Pd is embedded into the pyrolyzed polymeric structure, hence able to prevent sintering, while in C2, the metal is mainly on the surface of the pyrolyzed PAN nanoparticles, thus quite exposed to sintering. To prove that this is actually the case, a rather harsh thermal resistance test (TT) was performed on both catalysts, C1 and C2, which resulted in full sintering of the metal in the case of the C2 catalyst and only minimal sintering for C1. This is clearly shown in Figs. 7(a) and 7(b) by the Pd Lα EDX signal on the STEM graphs of the C1 and C2 catalysts, respectively: the much larger metal aggregates in the latter case prove the much larger extent of Pd sintering.

C. X-ray absorption characterization

Figure 8 shows the Pd K-edge X-ray absorption near edge structure (XANES) derived from a Pd foil (Pd(0)), the PANPd, and the pyrolyzed PANPd (PANPd PYR) samples. Surprisingly, we observe that PANPd has an edge position comparable to that of the Pd foil. Both extended X-ray absorption fine structure (EXAFS) analysis[29] and the UV-vis spectra shown in Fig. 3 would very much indicate that the Pd in PANPd is in fact Pd(II)—this is further established from a subsequent reanalysis of the PANPd EXAFS, which takes account of multiple scattering effects, present in the supplementary material.

In the first approximation, edge positions in X-ray Absorption Fine Structure can be attributed to the oxidation state of the metal center; i.e., the higher oxidation state shifts the absorption edge

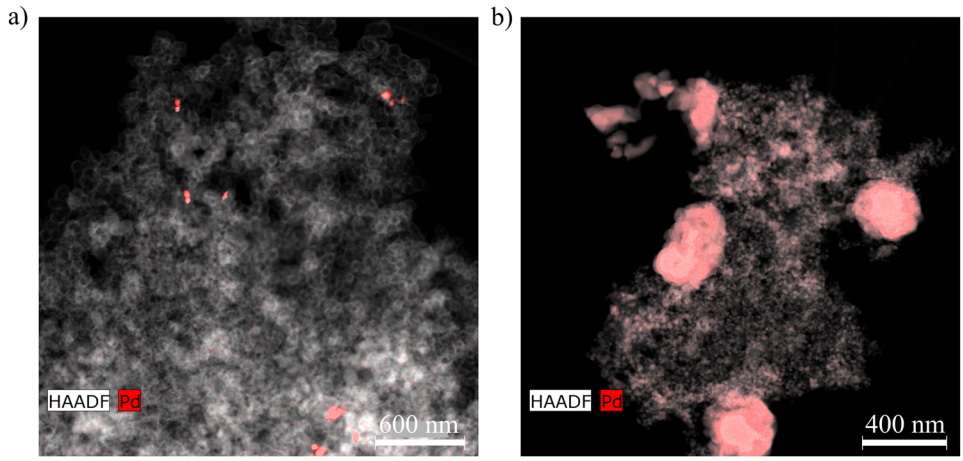

FIG. 7. STEM EDX of Pd Lα line on HAADF graphs after thermal resistance test (TT) after 200 h at 400 °C of (a) C1 catalyst and (b) C2 catalyst.

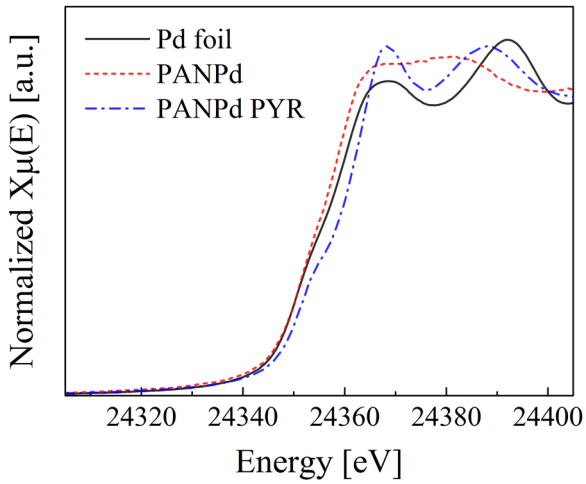

FIG. 8. X-ray absorption studies: normalized Pd K-edge XANES spectra of PANPd (red dashed line), PANPd PYR (blue dotted-dashed line), and Pd foil (black solid line).

towards higher energies. However, this is only one of several factors that may contribute to the energy position of an absorption edge. Charge transfer effects can also contribute to the position of the edge position and often in the opposite direction to that expected from only considering the formal charge existing at the metal centre itself.[45,46]

In the case of the PANPd sample, the Pd is bound to both Cl and N ligands. It has been previously demonstrated, for instance, that for $PdCl_2$, the energetic position of the Pd K-edge is shifted to lower bonding energies than would be expected on the basis of the formal charge associated with the Pd.[47] We might also consider that the N ligands may have the capacity to donate electron density to the Pd; the two effects may therefore combine and lead to total charge transfer effects that shift the energy position of the Pd K-edge to lower energies.

The XANES spectrum from the PANPd PYR sample is different again and appears to have characteristics that might be attributable to both Pd in a reduced state (a pronounced low energy shoulder commensurate with the binding energy of the Pd foil) and Pd that may have more of a Pd(II) character (the "white line" at ca. 24 368 eV). Given the nature of the pyrolysis, and that the samples have subsequently been exposed to air, a portion of the Pd resulting from the pyrolysis may have been oxidized. This seems likely and is consistent with the overall XANES envelope indicating the

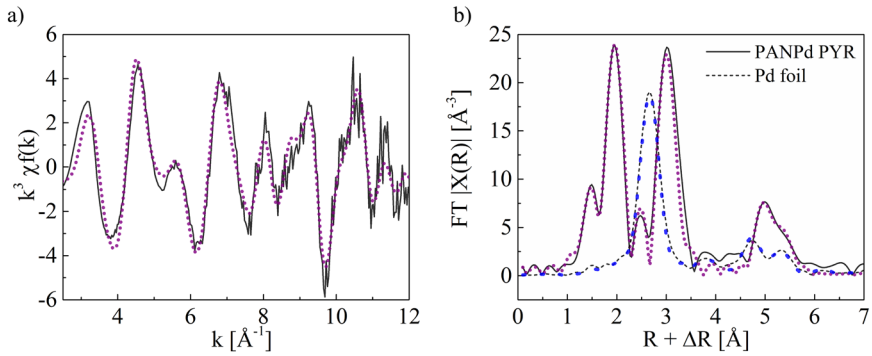

FIG. 9. X-ray absorption studies of PANPd PYR: (a) k^3-weighted EXAFS spectra of the imaginary part (black solid line) and fit (purple dotted line) and (b) Fourier transform (FT) k^3-weighted EXAFS spectra of the imaginary part of PANPd PYR (black solid line and fit as a purple dotted line) and Pd foil (black dashed line and fit as a blue dotted line).

presence of more than one phase—and oxidation state—of Pd in this sample but could also be the result of remaining Pd–N paths.

To further probe the nature of the Pd formed through the pyrolysis of PANPd, Pd K-edge EXAFS was measured. The resulting k^3-weighted EXAFS data and the corresponding Fourier transform are given in Fig. 9.

The EXAFS from the PANPd PYR sample shows a complex scattering envelope [Fig. 9(a)] that is then reflected in the Fourier transform [Fig. 9(b)]. What is most evident from both a visual inspection of the FT and the resulting analysis (Table II) is that the EXAFS from the PANPd PYR shows no scattering features that might indicate the presence of extended domains of either fcc Pd nanoparticles or PdO, the latter possessing a distinctive Pd–Pd shell structure with distances of 3.0 and 3.4 Å, respectively, that are entirely absent from the spectrum collected using a pyrolyzed sample of pure PAN. Furthermore, no evidence is forthcoming for the retention of Pd-Cl bonding post-pyrolysis as the path should be evident in the 2.3-2.4 Å range with a magnitude dependent on the disorder associated with it.

We note here that a number of shells can be fitted using both C and O scatterers with an essential equanimity. As such, values are given for the coordination and bond distances that arise from each case in Table II (with those parameters derived from replacing O with C being given in parentheses). Additionally, it is true that the last two shells of the fit could lack significance, but the features observed at higher k units in Fig. 9(a) are believed to be relevant.

Irrespective of the fitting of some shells using O or C, the principle Pd–Pd scattering shell at ca. 2.82 Å remains robust. Such a Pd–Pd scattering distance is significantly longer than that expected

TABLE II. Fitting parameters for the EXAFS spectrum of pyrolyzed PANPd (PANPd PYR), listed with increasing bond length.[a]

Sample	Shell	Bond length (Å)	Number of nearest neighbors (–)	Debye-Waller factor (Å^2)	R-factor (%)
PANPd PYR	Pd–C	1.5 (1.47)	0.4 (0.5)	0.011 (0.01)	33.37 (37.9)
	Pd–O/N/(C)	1.99 (2.04)	1.5 (2.7)	0.004 (0.004)	
	Pd–Pd	2.82 (2.82)	1.7 (1.5)	0.014 (0.012)	
	Pd–O(C)	2.89 (2.94)	5.1 (6.8)	0.015 (0.0010)	
	Pd–O2 (C)	4.93 (5.11)	6.9 (9)	0.014 (0.009)	
	Pd–Pd2	5.11 (5.11)	3.2 (2.2)	0.012 (0.009)	

[a]$E_F = -6.5$ is the edge position relative to the vacuum zero (E_F = Fermi energy); R-factor = $(\int|\chi^T - \chi^E|k^3dk/|\chi^E|k^3dk) \times 100\%$, where χ^T and χ^E are the theoretical and experimental EXAFS, respectively, and k is the photoelectron wave vector; the Debye–Waller factor = $2\sigma^2$, where σ is the root mean square internuclear separation; the structural data are obtained using k-range = 2.5–13 Å^{-1}; AFAC = 0.9 is related to the proportion of electrons performing an EXAFS type scatter on absorption. Errors in the bond distance and the number of nearest neighbors may be considered at approximately 1.5% and 10%, respectively, of the state value.

for Pd nanoparticles (<2.75 Å).[48] However, this would be consistent with the presence of carbide nanoparticulate PdC_x, while hydrides (PdH_x) are typically not stable above 100 °C.[48–51] We further note that previous studies of such materials using EXAFS have shown both a considerable reduction in the intensity of the first Pd–Pd shell (relative to the case of pure Pd metal) and a complete absence of the expected fcc second Pd-Pd shell (ca. 3.89 Å), and the same observations could equally apply to the PANPd PYR case.

Furthermore, given the nature of both the support and the pyrolysis, it would not seem unreasonable to expect that any Pd nanoparticles formed would be predominantly attached to, and then contain, carbon. The balance of evidence from the EXAFS would therefore suggest that a significant proportion of the Pd created through pyrolysis of PANPd exists as a very highly dispersed PdC_x phase in close contact with an essentially graphitic support.

The fitting of a short (ca. 1.5 Å) Pd–C scatter might be speculatively explained through a Pd adsorbed in threefold hollow carbon sites that could exist at the surface of such PdC_x phases. The fitting of this shell is statistically significant to the overall fit even though previous studies concerning both bulk and nanoparticulate (ca. 5 nm) PdC_x entities have not reported such a scattering interaction.

The higher (>4.5 Å) shells fitted are difficult to explain (no similar data were found in the literature) and, more specifically, data length and overall quality are out of the allowable range. However, they appear with an intensity in the EXAFS and FT that is unusual, one that would indicate a degree of order being present in the components suggested in the XANES. It should be noted that there is no evidence for shell progressions that we can easily associate with an extended fcc or PdO phase. We might only speculate that these well-defined interactions could arise from one or other Pd components having an ordered, possibly two-dimensional extension, over the (essentially) graphitic support. Unfortunately, such a precise specification of the structure of these species is not possible from the currently available data.

To summarize, the EXAFS analysis indicates that the result of the pyrolysis is not easily ascribable to the formation of a single Pd species. The evidence does however strongly suggest that a significant proportion of the Pd present shows characteristics in EXAFS that would be consistent with a very highly dispersed PdC_x phase that may coexist with another more oxidized phase of a structure that cannot be precisely determined from these measurements. On the other hand, this unknown phase could also result from original Pd-N bonds still present in PANPd PYR. In fact, a previous study of pyrolyzed PAN CPs showed that a nitrogen content of about 6% is still present after pyrolysis.[28]

D. Catalysis: Suzuki cross coupling

As C1 and C2 have a similar support in terms of chemical structure (ladder structure containing carbon and nitrogen) but different Pd spatial distribution, their comparison in terms of catalytic activity could be of interest. With this aim, a cross coupling reaction, Suzuki coupling, carried out in the liquid phase was selected as the benchmark reaction.

The results of the Suzuki cross coupling reactions employing the two aforementioned different catalysts are shown in Fig. 10. As anticipated, two different cases are examined at 90 °C: (i) PANPd PYR reduced, C1, and (ii) wet-impregnated pyrolyzed PAN with 3.5 wt. % Pd, C2. The catalytic performances are quantified in terms of R [see Eq. (1)], which results from the conversion of the aryl bromide (limiting reactant) with respect to the product as measured by ^{1}H NMR (two repetitions).

The same reaction was also performed at 80 and 100 °C but resulted in a limited effect of the temperature in this particular range, independent of the specific catalyst (refer to the supplementary material for more details). Looking at the results in Fig. 10, the most active catalyst right after preparation is C2, probably due to the complete accessibility of the Pd nanoparticles on the surface of the support. Nevertheless, the C1 catalyst still shows good activity given the probable smaller active site accessibility.

The thermal resistance test (TT) was meant to simulate the aging of the catalysts but resulted in an important activity increase and decrease for C1 and C2, respectively (see Fig. 10). These observations are consistent with the STEM micrographs shown in Fig. 7. While the activity of C2

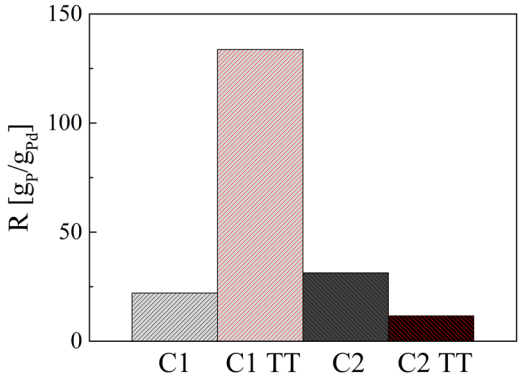

FIG. 10. Ratio *R* [cf. Eq. (1)] describing the extent of the reaction at 90 °C, for the catalysts C1 and C2 as prepared as well as after a thermal resistance test (TT), C1 TT, and C2 TT.

was decreasing given the severe sintering of the surface Pd nanoparticles, the Pd incorporated in C1 is much more stable and its activity is actually greatly improved. In both cases, the weight loss after TT was high, about 74% and 62% for C1 and C2, respectively. On the one hand, this is expected given the harsh conditions of the treatment and its long duration. On the other hand, more porosity is created, giving access to buried Pd in the case of C1, while more Pd sintering takes place on the surface of C2. We can also conclude that the pyrolysis step at higher temperature does not lead to a finished material in terms of weight loss and porosity creation. Thus, one could think about optimizing this specific step to improve the activity of the C1 catalyst. Moreover, it has to be stated that the TT experiments were only performed once given the long synthetic procedure. In addition, the direct use of dispersed metal nanoparticles was applied to provide another reference case (see the supplementary material). All these results are reported in numerical form in Table 2S of the supplementary material.

Therefore, comparing R between C1TT and C2TT in Fig. 10, one may draw some conclusions about the thermal behavior. Before TT, we have observed that *R* is slightly lower for C1 than for C2, which was explained by lower accessibility of Pd in C1. After TT, the substantially higher *R* value for C1TT than for C2TT obviously results from two factors. First, the accessibility of Pd in C1TT has been increased. Second, sintering of Pd atoms in C1TT is insignificant, while it is very strong in C2TT, leading to substantial reduction in activity. Thus, this result clearly confirms the advantages of the present approach for metal incorporation with respect to the conventional wet-impregnation.

IV. CONCLUSIONS

Porous polymer powders have been prepared by aggregation of polyacrylonitrile nanoparticles incorporating palladium. The spatial distribution of the noble metal inside the nanoparticles could be controlled by applying suitable semi-batch reaction conditions, as proposed in a previous study.[29] The resulting catalyst exhibits macropores with a diameter of about 100 nm, while much smaller pores (0.7-5 nm) have been created into the nanoparticles by pyrolysis. In this respect, quite harsh conditions were required, involving the use of KOH as the pyrolytic activator and temperature up to 800 °C. Starting from metal contents of about 0.5 wt. % before pyrolysis, the Pd content in the final catalyst was quite large, 2.8 wt. %, despite an overall mass loss up to 80% suffered by the material during the thermal treatment. During pyrolysis, two different phases of Pd are formed in a highly dispersed manner: PdC_x and another unknown oxidized structure, which could still be remaining Pd-N bonds from the original PANPd, as confirmed by XANES and EXAFS.

For the sake of comparison, a second catalyst was synthesized following the same strategy (colloidal aggregation and thermal treatment up to 900 °C) but using metal-free PAN CPs and loading the noble metal by conventional wet impregnation. The final material (C2) resulted in the formation of extremely small and fully accessible Pd nanoparticles on the surface of the support. Then, a thermal

resistance test was performed on both C1 and C2, showing the much faster sintering of the noble metal nanoparticles in the case of the catalyst prepared by wet impregnation, C2, while minimal sintering only was observed in the case of C1.

Finally, the catalytic activity of both aforementioned catalysts was tested using a Suzuki coupling reaction as the model system. Both supported catalysts C1 and C2 provided good values of final conversion of the aryl bromide. Additionally, this thermal resistance test also provided more access to isolated Pd in C1, hence increasing greatly the conversion of the limiting reactant.

To sum up, the proposed synthetic strategy appears to be effective to incorporate the metal and prevent sintering while offering good enough accessibility to reactants. These properties, combined with the very cheap support material and an easily scalable synthesis, make the proposed synthetic strategy meaningful and the resulting material worthy of further applications.

SUPPLEMENTARY MATERIAL

See supplementary material for more details on the thermal treatment (porosity), EXAFS fitting of PANPd and PANPd PYR, EDX elemental maps, and all results of the Suzuki and NMR spectra of the obtained product.

ACKNOWLEDGMENTS

The financial support from the Swiss National Science Foundation (Grant No. 200020_165917) is gratefully acknowledged. The authors thank the Swiss Light Source for the provision of beamtime at the SuperXAS beamline. Additionally, the authors thank Dr. Tigran Magrossian for the access and sound advices on the UV-vis results, Marcel Lorenz for discussions, and Leslie Riwar for her help in purifying 4-methylbiphenyl after the Suzuki coupling.

[1] D. Astruc, F. Lu, and J. R. Aranzaes, Angew. Chem., Int. Ed. **44**, 7852 (2005).
[2] J. D. A. Pelletier and J. M. Basset, Acc. Chem. Res. **49**, 664 (2016).
[3] P. Munnik, P. E. De Jongh, and K. P. De Jong, Chem. Rev. **115**, 6687 (2015).
[4] J. Liu, ACS Catal. **7**, 34 (2017).
[5] J. Grunes, J. Zhu, and G. A. Somorjai, Chem. Commun. **2003**, 2257.
[6] M. Pagliaro, V. Pandarus, R. Ciriminna, F. Béland, and P. DemmaCarà, ChemCatChem **4**, 432 (2012).
[7] N. Semagina and L. Kiwi-Minsker, Catal. Rev. **51**, 147 (2009).
[8] X. F. Yang, A. Wang, B. Qiao, J. Li, J. Liu, and T. Zhang, Acc. Chem. Res. **46**, 1740 (2013).
[9] S. Abbet, A. Sanchez, U. Heiz, W. D. Schneider, A. M. Ferrari, G. Pacchioni, and N. Rösch, J. Am. Chem. Soc. **122**, 3453 (2000).
[10] B. Qiao, A. Wang, X. Yang, L. F. Allard, Z. Jiang, Y. Cui, J. Liu, J. Li, and T. Zhang, Nat. Chem. **3**, 634 (2011).
[11] S. Sun, G. Zhang, N. Gauquelin, N. Chen, J. Zhou, S. Yang, W. Chen, X. Meng, D. Geng, M. N. Banis, R. Li, S. Ye, S. Knights, G. A. Botton, T.-K. Sham, and X. Sun, Sci. Rep. **3**, 1775 (2013).
[12] S. Yang, Y. J. Tak, J. Kim, A. Soon, and H. Lee, ACS Catal. **7**, 1301 (2017).
[13] J. M. Thomas and R. Raja, Top. Catal. **40**, 3 (2006).
[14] S. Liang, C. Hao, and Y. Shi, ChemCatChem **7**, 2559 (2015).
[15] A. Zecchina, S. Bordiga, and E. Groppo, in *Selective Nanocatalysts and Nanoscience*, 1st ed., edited by A. Zecchina, S. Bordiga, and E. Groppo (Wiley-VCH Verlag GmbH & Co. KGaA, 2011), pp. 1–27.
[16] T. Imaoka, Y. Akanuma, N. Haruta, S. Tsuchiya, K. Ishihara, T. Okayasu, W.-J. Chun, M. Takahashi, and K. Yamamoto, Nat. Commun. **8**, 688 (2017).
[17] K. Larmier, W. C. Liao, S. Tada, E. Lam, R. Verel, A. Bansode, A. Urakawa, A. Comas-Vives, and C. Copéret, Angew. Chem., Int. Ed. **56**, 2318 (2017).
[18] E. Lam and J. H. T. Luong, ACS Catal. **4**, 3393 (2014).
[19] A. Tuel, Microporous Mesoporous Mater. **27**, 151 (1999).
[20] J. G. McCarty, M. Gusman, D. M. Lowe, D. L. Hildenbrand, and K. N. Lau, Catal. Today **47**, 5 (1999).
[21] Y. Cao, S. Mao, M. Li, Y. Chen, and Y. Wang, ACS Catal. **7**, 8090 (2017).
[22] Y. Guo, A. Solovyov, N. A. Grosso-Giordano, S. J. Hwang, and A. Katz, ACS Catal. **6**, 7760 (2016).
[23] K. Matyjaszewski and J. Spanswick, Mater. Today **8**, 26 (2005).
[24] R. Mülhaupt, Angew. Chem., Int. Ed. **43**, 1054 (2004).
[25] J. Przepiórski, M. Skrodzewicz, and A. W. Morawski, Appl. Surf. Sci. **225**, 235 (2004).
[26] M. Telychko, P. Mutombo, M. Ondráček, P. Hapala, F. C. Bocquet, J. Kolorenč, M. Vondráček, P. Jelínek, and M. Švec, ACS Nano **8**, 7318 (2014).
[27] M. S. A. Rahaman, A. F. Ismail, and A. Mustafa, Polym. Degrad. Stab. **92**, 1421 (2007).
[28] A. Beltzung, A. Klaue, C. Colombo, H. Wu, G. Storti, and M. Morbidelli, Energy Technol. **6**, 718 (2018).
[29] A. Beltzung, C. Colombo, M. Nachtegaal, H. Wu, G. Storti, and M. Morbidelli, Polymer **145**, 41 (2018).
[30] N. Binsted, PAXAS: Program for the Analysis of X-Ray Absorption Spectra, University of Southampton, 1998.

[31] N. Binsted, EXCURV98, CCLRC Daresburry Laboratory Computer Program, 1998.
[32] F. Wen, W. Zhang, G. Wei, Y. Wang, J. Zhang, M. Zhang, and L. Shi, Chem. Mater. **20**, 2144 (2008).
[33] H. Wu and M. Morbidelli, Particuology **14**, 1 (2014).
[34] S. Pande and R. M. Crooks, Langmuir **27**, 9609 (2011).
[35] N. K. Sharma, R. K. Ameta, and M. Singh, Biochem. Res. Int. **2016**, 4359375.
[36] S. Seyfi, R. Alizadeh, M. D. Ganji, and V. Amani, Polyhedron **134**, 302 (2017).
[37] T. Krigas and M. T. Rogers, J. Chem. Phys. **54**, 4769 (1971).
[38] S. Eden, P. Limão-Vieira, P. Kendal, N. J. Mason, S. V. Hoffmann, and S. M. Spyrou, Eur. Phys. J. D **26**, 201 (2003).
[39] H. Zhang, L. Xu, F. Yang, and L. Geng, Carbon **48**, 688 (2010).
[40] T. Lopez, M. Villa, and R. Gomez, J. Phys. Chem. **95**, 1690 (1991).
[41] J. Wang, I. Senkovska, M. Oschatz, M. R. Lohe, L. Borchardt, A. Heerwig, Q. Liu, and S. Kaskel, J. Mater. Chem. A **1**, 10951 (2013).
[42] Y. K. Kim, G. M. Kim, and J. W. Lee, J. Mater. Chem. A **3**, 10919 (2015).
[43] M. Sevilla, P. Valle-Vigón, and A. B. Fuertes, Adv. Funct. Mater. **21**, 2781 (2011).
[44] G. Sethia and A. Sayari, Carbon **93**, 68 (2015).
[45] K. Shimizu, Y. Kamiya, K. Osaki, H. Yoshida, and A. Satsuma, Catal. Sci. Technol. **2**, 767 (2012).
[46] A. "Bean" Getsoian, U. Das, J. Camacho-Bunquin, G. Zhang, J. R. Gallagher, B. Hu, S. Cheah, J. A. Schaidle, D. A. Ruddy, J. E. Hensley, T. R. Krause, L. A. Curtiss, J. T. Miller, and A. S. Hock, Catal. Sci. Technol. **6**, 6339 (2016).
[47] M. Tromp, J. A. Van Bokhoven, G. P. F. Van Strijdonck, P. W. N. M. Van Leeuwen, D. C. Koningsberger, and D. E. Ramaker, J. Am. Chem. Soc. **127**, 777 (2005).
[48] M. W. Tew, J. T. Miller, and J. A. van Bokhoven, J. Phys. Chem. C **113**, 15140 (2009).
[49] J. A. McCaulley, Phys. Rev. B **47**, 4873 (1993).
[50] J. A. McCaulley, J. Phys. Chem. **97**, 10372 (1993).
[51] A. Rose, S. Maniguet, R. J. Mathew, C. Slater, J. Yao, and A. E. Russell, Phys. Chem. Chem. Phys. **5**, 3220 (2003).